CRREL

LEVEL ①

REPORT 81-11

Prediction of explosively driven
relative displacements in rocks
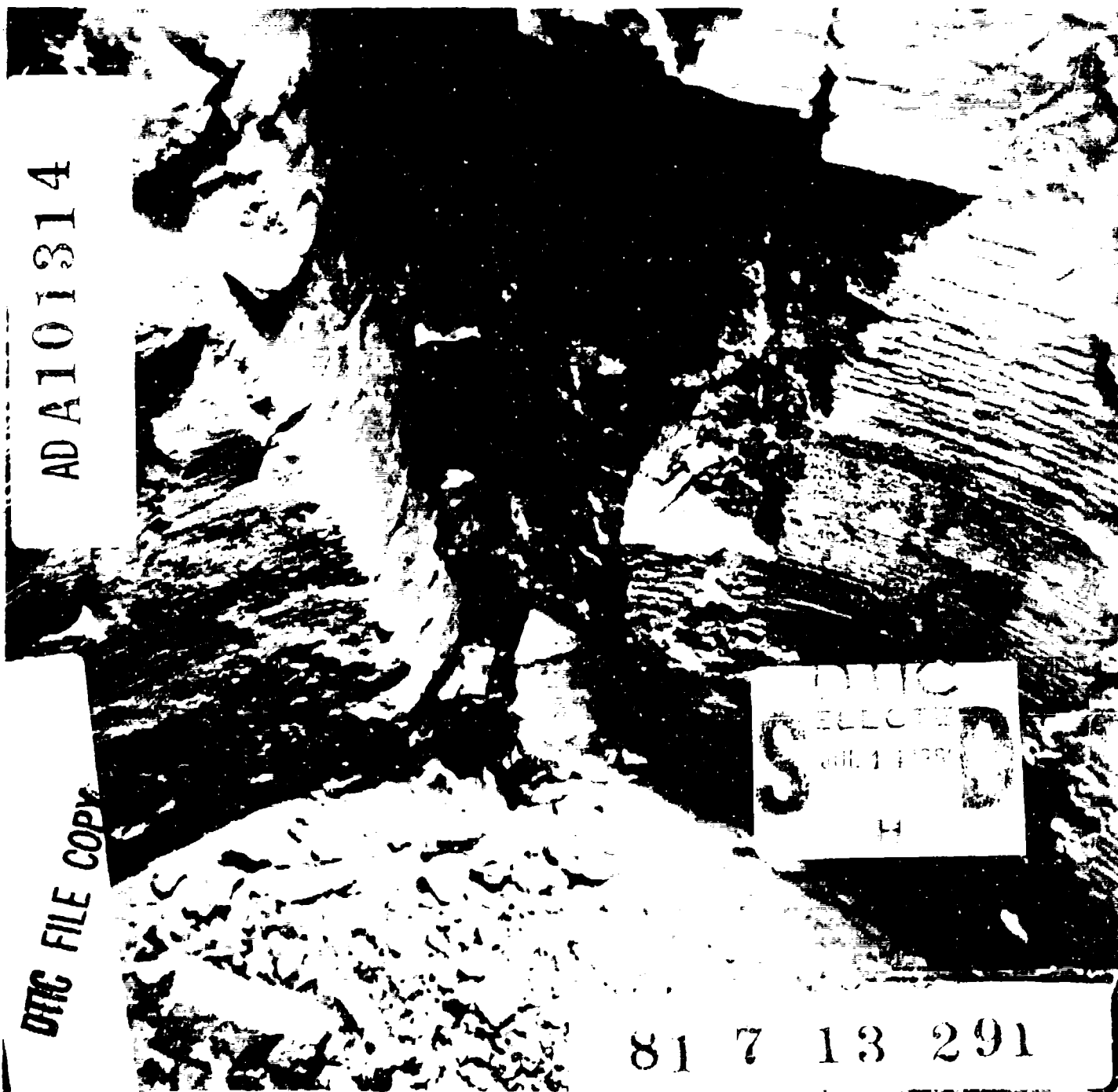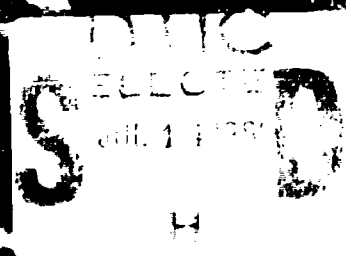
81 7 13 291

Cover: Damage to unlined structure in hard rock resulting from explosive loading.

CRREL Report 81-11

Prediction of explosively driven relative displacements in rocks

Scott Blouin

June 1981

Accession For
NTIS GRA&I
DTIC TAB
Unannounced
Justification

By
Distribution/
Availability Codes
Dist | Avail and/or Special

A

REPORT DOCUMENTATION PAGE		READ INSTRUCTIONS BEFORE COMPLETING FORM
1. REPORT NUMBER CRREL Report 81-11	2. GOVT ACCESSION NO. AD-A101 314	3. RECIPIENT'S CATALOG NUMBER
4. TITLE (and Subtitle) PREDICTION OF EXPLOSIVELY DRIVEN RELATIVE DISPLACEMENTS IN ROCKS		5. TYPE OF REPORT & PERIOD COVERED
		6. PERFORMING ORG. REPORT NUMBER
7. AUTHOR(s) Scott Blouin		8. CONTRACT OR GRANT NUMBER(s) AFWL Orders no. 76-220, 76-298, 77-182, 78-099, 78-165
9. PERFORMING ORGANIZATION NAME AND ADDRESS U.S. Army Cold Regions Research and Engineering Laboratory Hanover, New Hampshire 03755		10. PROGRAM ELEMENT, PROJECT, TASK AREA & WORK UNIT NUMBERS
11. CONTROLLING OFFICE NAME AND ADDRESS U.S. Air Force Weapons Laboratory Kirkland AFB, New Mexico 87117		12. REPORT DATE June 1981
		13. NUMBER OF PAGES 26
14. MONITORING AGENCY NAME & ADDRESS(if different from Controlling Office)		15. SECURITY CLASS. (of this report) Unclassified
		15a. DECLASSIFICATION/DOWNGRADING SCHEDULE

16. DISTRIBUTION STATEMENT (of this Report)

Approved for public release; distribution unlimited.

17. DISTRIBUTION STATEMENT (of the abstract entered in Block 20, if different from Report)

18. SUPPLEMENTARY NOTES

19. KEY WORDS (Continue on reverse side if necessary and identify by block number)

Block motion   Relative displacement
Explosion effects Rock mechanics
Fault motion   Rock dynamics
Ground motion
Nuclear weapons effects

20. ABSTRACT (Continue on reverse side if necessary and identify by block number)

Relative displacement data from high explosive, shallow-buried bursts in rock are combined with relative displacement data from the contained nuclear explosion MIGHTY EPIC. Analysis of these data yields a preliminary, semi-empirical technique for predicting the location, direction and magnitude of elastic displacements in rock from contained explosions. This technique is used to make relative displacement predictions for the DIABLO HAWK nuclear blast.

DD FORM 1473 EDITION OF 1 NOV 65 IS OBSOLETE
1 JAN 73

PREFACE

CONTENTS

ILLUSTRATIONS

TABLES

PREDICTION OF EXPLOSIVELY DRIVEN RELATIVE DISPLACEMENTS IN ROCKS

Scott Blouin

INTRODUCTION

Deep-based defense systems, such as a reserve ballistic missile force or command control and communications facilities, buried in rock at depths of half a kilometer or more, hold promise as relatively invulnerable future links in United States strategic defenses. One of the key uncertainties in deep basing, however, is the possible susceptibility of these systems to relative displacements of rock, or block motions, which occur well beyond the crater caused by surface or shallow-buried nuclear explosions. Considerable experimental evidence of rock displacement has been gathered following both high explosive and underground nuclear detonations.

Experimental studies of the feasibility of siting missile silos in rock during the Hard Rock Silo Program —conducted by the Air Force and the Defense Atomic Support Agency in the late 60's and early 70's—demonstrated that a principal threat to the silos was from explosion-induced displacement of large rock masses or blocks along pre-existing planes of weakness in the in situ rock. These relative motions were observed along bedding planes, joints, joint sets, and interfaces between different rock types, in both igneous and sedimentary rocks. In instances where they intersected concrete and steel-lined structures, the structures were sheared in direct proportion to the displacement in the free-field.

The high explosive test series which drove these displacements is described by Blouin (1980). The test technique (having the acronym DIHEST, for Direct Induced High Explosive Simulation Technique) employed a buried vertical array of high explosives, simultaneously detonated, to generate ground motions

thought to be similar to those created by the cratering action of a nuclear surface burst. The DIHEST shots all produced elliptically shaped craters with their long axes in line with the explosive arrays. Relative displacements were observed to nearly three crater radii from the arrays. They were also observed at depths below the bottom of the craters, though no attempt was made to determine the maximum extent of these displacements at depth. It is important to note that of the multitude of relative displacements documented during this program, perhaps only one would have been observed during a casual post-shot examination. The rest were discovered following the extensive debris clearance and excavation needed to recover survey points on the test bed surface or to document structural damage. The magnitudes of the relative displacements observed during this test series ranged from less than 1 cm to 4 m.

The recent underground nuclear shot MIGHTY EPIC conclusively demonstrated that explosively driven relative displacements of considerable magnitude occur at great depths. Short and Kennedy (1978) and Townsend (1976, 1977 a,b,c) document at least seven instances of relative displacement along faults, bedding planes, and an interface between adjoining rock types. The magnitudes of these displacements ranged from 0.4 m to more than 1.7 m. Several test structures were severely damaged by these displacements.

Clearly, the viability of any deep-based defense system must partially rest on a credible demonstration that the system will not be vulnerable to these types of relative displacement. Design must follow one or a combination of three approaches. First, the system may be located below the maximum depth

to which block motion will be propagated by the expected threat (surface or shallow-buried bursts). Second, the system may be designed to "absorb" the anticipated relative displacements. Third, the rock discontinuities might be reinforced using rock bolts, grout or some other means to reduce or eliminate the anticipated displacements. All three approaches, however, are dependent on predictions of the extent, magnitude, and direction of the relative displacements, or on the shear stresses which generate them. In addition design of critical communications links, access tunnels and shafts, etc. will also depend on a credible block-motion prediction technique. In short, such predictions will be critical to feasibility studies and subsequently to nearly all aspects of the design of any deep-based system.

This report summarizes an initial attempt to formulate a semi-empirical procedure for predicting the maximum extent, direction and magnitude of relative displacements resulting from an underground nuclear detonation in the Nevada Test Site tuff. Specifically, such predictions are derived for every fault documentation station of the underground nuclear shot DIABLO HAWK, detonated in September 1978. This effort is envisioned as a principal logical step toward the ultimate goal of providing credible predictions of the relative displacements at depth which result from surface or shallow-buried nuclear explosions.

The prediction procedures described herein are based on relative displacement data from the DIHEST HE (high explosive) events and the MIGHTY EPIC underground nuclear shot. All displacements used in the analyses are of the "driven" variety; that is, the direction of slip is in the general direction of the maximum dynamic shear stress generated by the explosion. So called "triggered" displacements, where the direction of motion is in the direction of the maximum in situ shear stress, are not treated here (for a further discussion of triggered motions, see Bache and Lambert 1976). Analyses of both the relevant DIHEST data and MIGHTY EPIC data are presented, along with the many assumptions and approximations involved in the formulation of the prediction procedures. Finally, details of the DIABLO HAWK prediction procedures are summarized and the individual predictions at each fault documentation station are presented.

The predictions are made in two parts. First, probable slip locations and directions are identified through an analysis procedure which superimposes an approximation of the dynamic, explosion-generated stresses on the in situ stresses. Once probable slip locations are identified, the magnitudes of the displacements expected at these locations are determined through a semi-empirical conservation of energy relationship.

DIHEST ANALYSIS

The DIHEST series produced significant block motions in five out of seven events. Though no attempt was made to monitor displacements beneath the explosive arrays, the near-surface data are valuable in that a fairly complete definition of the extent and geometry of the block movements could be made from the combined test bed and structural surveys, a definition which is much more complete than is possible in the underground environment. In addition, the large number of ground-motion instrument locations provided good ground-motion data on both sides of the slip planes, whereas the underground data are more sparse, tend to be of poorer quality and are inconclusive (see, for example, Short and Kennedy 1978). An example of the DIHEST ground motion data which are suggestive of the mechanisms controlling the magnitude of those displacements is shown in Figure 1. A comparison of horizontal velocity time histories is shown for near-surface gage locations on the STARMET event. The gage at the 9.1-m range from the explosive array was located within a large block of rock which was upthrust along a joint or joint set dipping toward the array at an angle of 67°. The gage at the 18.3-m range was located beyond this slip surface. It is obvious from the time histories that relative motion began at, or soon after, passage of the initial velocity peak—which should correspond closely to passage of the peak dynamic stress. By the time the 18.3-m gage had come to rest (at about 0.1 s) the 9.1-m gage was still moving outward at nearly peak velocity. This velocity was then gradually slowed at a nearly constant rate, suggesting application of a constant restraining force to the sliding block. Total permanent horizontal displacement at the 18.3-m gage was negligible, while that at the close-in gage was 0.51 m. Both displacements agree closely with post-shot survey data.

In this case the data comparison suggests that once relative displacement begins, the thrust block may be considered a free body sliding up the slip surface at an initial velocity equal to the vector sum of the peak horizontal and vertical velocities. The constant restraining force is supplied by gravity acting on the block, plus a friction force between the block and slip plane resisting the upward slide. Such a block model is shown schematically in Figure 2. The kinetic energy of the block is thus expended in the form of work against the forces of gravity and friction. The work done against gravity can be expressed as a change in potential energy of the block,

2
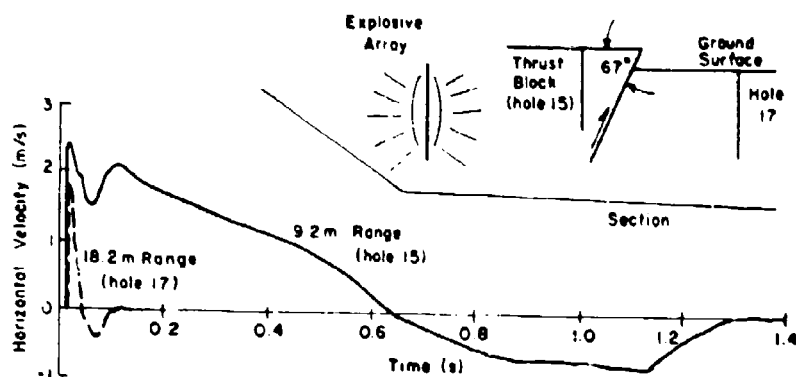
Figure 1. STARMET velocity time history comparison.
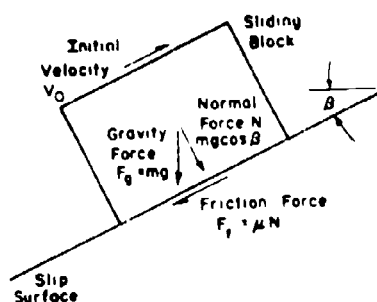
Figure 2. Schematic of DIHEST block model.

given by

$$\Delta E_p = mg \, \delta \, \sin\beta \qquad (1)$$

where m is the mass of the block, g the acceleration of gravity, and $\delta \sin\beta$ the vertical component of total displacement along the slip plane, where β is the dip angle of the slip surface. The work done against friction equals the friction force multiplied by the total displacement along the slip plane, which is given by

$$\Delta E_f = \mu \, mg \, \delta \, \cos\beta \qquad (2)$$

where μ is the coefficient of sliding friction between the block and slip plane. The normal force on the slip plane, $mg \cos\beta$, is assumed to be due only to the weight of the block. Summing eq 1 and 2 and setting them equal to the initial kinetic energy of the block yields

$$\tfrac{1}{2}mv_0^2 = mg \, \delta \, \sin\beta + \mu \, mg \, \delta \, \cos\beta \qquad (3)$$

where v_0 is the vector sum of the peak horizontal and vertical velocities. Rearranging gives an expression for

the total displacement δ of

$$\delta = \frac{v_0^2}{2g(\mu \cos\beta + \sin\beta)} \qquad (4)$$

Table 1 summarizes the most dramatic relative displacements observed in the DIHEST series. Motion generally occurred along joints or joint sets striking approximately parallel to the explosive array and dipping toward it. PLANEWAVE II was an exception in that motion occurred along bedding planes and lithologic interfaces having essentially no dip. HANDEC II was also an exception, as motion occurred along a joint dipping away from the explosive array. The last column of Table 1 shows the relative displacements calculated using eq 4. The resultant peak velocities used in the calculations and listed in the table were calculated using the average peak horizontal and vertical velocities at the range where each slip plane intersected the testbed surface. The coefficient of friction was assumed at 0.5, a typical value for many faults.

For all events but DATEX II, eq 4 overpredicts the total displacement. This would be expected for

3

Table 1. DIHEST relative displacement summary.

Event Rock type Seismic velocity (m/s)	DIHEST yield (kg) (tons)	Max rel displ (m) Range (m) Dip angle β	Avg. peak particle velocity (m/s)			Displ from eq 4 μ = .5 (m)
			Horizontal	Vertical	Resultant	
PLANEWAVE II Interbedded sedimentary 1220 – 3050	1905 (2.1)	<0.1 17.4 ≅ 0°	2.0*	–	>2.0	0.4**
STARMET Granite 3650 – 5180	1995 (2.2)	1.7 12.8 67°	4.6	4.6	6.5	1.9
DATEX II Tonalite 2130 – 3660	37,190 (41)	4.0 33.5 ≅ 20°	4.6*	2.3*	5.1*	1.6
HANDEC II Tonalite 2130 – 3660	41,725 (46)	0.8 36.6 – 30°	6.1	2.9	6.8	2.5**
ROCKTEST II Tonalite 2130 – 3660	106,120 (117)	0.3 68.6 20°	2.9	1.5	3.3	0.7

* Estimated value.
** Equation applied, though recognized that assumptions governing its derivation do not hold in this case.

PLANEWAVE II and HANDEC II, where the respective horizontal and negative dip of the slip plane geometry tends to restrict slip more than the geometry of the model used to derive the equation. The overprediction on STARMET is minimal; the agreement between calculated and actual displacement is excellent. A factor contributing to the overprediction of displacement for both ROCKTEST II and HANDEC II was that during displacement a considerable air overpressure had been applied to the testbeds to simulate the concurrent nuclear airblast. In the case of HANDEC II, it is esimated (Blouin 1980) that air overpressure on the testbed was close to 70 bars at the arrival of the compression wave from the DIHEST explosion and that the overpressure had dropped to approximately 15 bars by the completion of relative displacement. The ROCKTEST II overpressure is classified, but it too was substantial. The combined effects of the airblast and airblast-induced ground motions on the relative displacements are complicated and beyond the scope of this work. Qualitatively at least, it appears likely that they tended to reduce the magnitude of slip, though not to the extent the first order approximations would indicate.

A closer look at the STARMET ground motion data reveals that the good agreement between calculated and measured relative displacements is somewhat misleading, but at the same time it is indicative

of a mechanism which would explain the large underprediction of displacement on DATEX II—where, unfortunately, no ground motion measurements were taken in the vicinity of the displacements. Figure 3 shows the vertical velocity time history from hole 15 within the STARMET thrust block, the companion to the horizontal time history of Figure 1. Starting at approximately 0.1 s (just beyond the velocity peak) and lasting for more than 0.5 s, a gradual steady deceleration of the block occurred. As indicated, the slope of this portion of the time history is –1g, implying that gravity alone was responsible for the deceleration of the block. The displacement hodograph of Figure 4 was constructed from the horizontal and vertical displacement time histories. It shows that the thrust block moved upward and outward along the slip plane, which dipped 67° toward the explosive array, reaching a peak displacement at this point of 2.0 m. The block then slid back down the boundary joint, coming to rest at a final displacement of 1.4 m. Using the peak 2.5- and 5.3-m/s horizontal and vertical velocities from the time histories in Figures 1 and 3 in eq 4 gives a value of displacement of 1.9 m for a friction coefficient of zero and a value of 1.6 m for a coefficient of 0.5. The first value is in excellent agreement with the 2.0-m actual peak displacement while the second value agrees well with the 1.4-m permanent displacement. However, it is obvious that the latter agreement
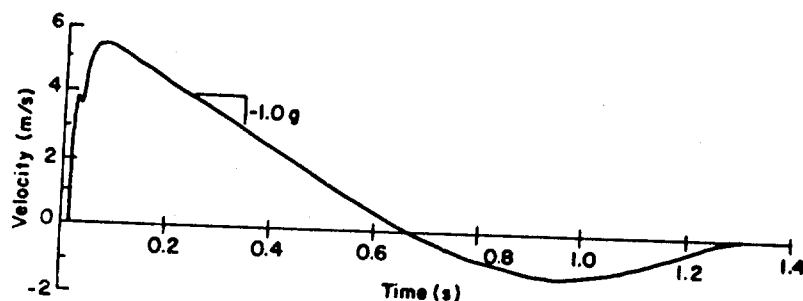
4

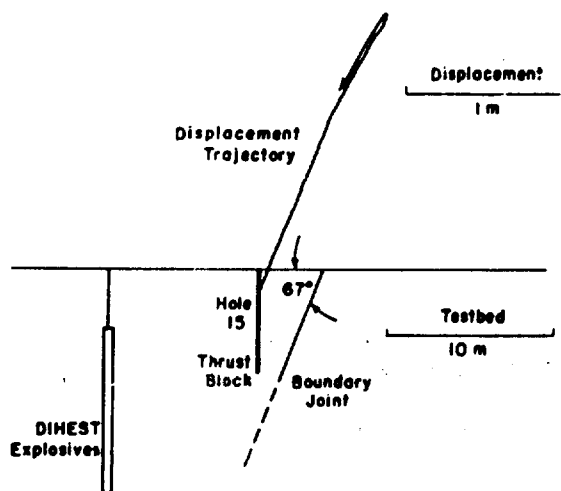Figure 3. STARMET thrust block—hole 15 vertical velocity.

Figure 4. Section schematic –hole 15 displacement trajectory.

is simply fortuitous because the block slid back down the slip plane and happened to finally come to rest at a 1.4-m displacement. Thus it appears that the block was actually in spall, driven upward and outward by the explosion along the direction of the slip surface, but with little or no normal force on the joint during the outward transition.

If this assumption is applied to the DATEX II maximum displacement, eq 4 then indicates a 3.9-m peak displacement when using zero for the friction coefficient. This is very close to the actual permanent displacement of 4.0 m. Furthermore, for a coefficient of friction of 0.5, the minimum slip surface dip which would allow a block to slide back down the slip surface under the force of gravity is 26.6°. Thus, because of its low dip angle, the DATEX II block would not have slid back down the boundary joint as the STARMET block did, making its permanent displacement and peak displacement essentially equal.

In conclusion, it appears that the conservation of block energy, using the peak resultant velocity to calculate the initial kinetic energy of the block, is a

valid approach for predicting the displacement of blocks which intersect the free surface. Due to the explosion and/or ground motion geometry, the frictional resistance to sliding may be negligible, and in some instances the blocks appear to be in a state of spall. Use of eq 4 with a coefficient of friction of zero serves as an upper bound to all the DIHEST relative displacements. For STARMET and DATEX II, the upper bound is a good fit to the actual peak displacements. For HANDEC II and ROCKTEST II, where the DIHEST test was combined with a nuclear airblast simulation, the interaction of the air overpressure and of the resulting airblast-induced ground motions with the DIHEST-induced relative displacements appear to have somewhat restrained the block motion.

MIGHTY EPIC ANALYSIS

Geological setting and relative displacement documentation

The MIGHTY EPIC underground nuclear detonation produced six documented instances of relative displacement along faults and bedding planes in the Rainier Mesa tuff. In most instances both the dip and strike components of slip were determined. In addition, relative movement was detected along the interface between the tuff and an underlying quartzite, but since this motion was within or adjacent to a rubble zone which is not close to the location of the DIABLO HAWK event, it was not incorporated into the MIGHTY EPIC relative displacement analysis.

Only a brief description of the MIGHTY EPIC/ DIABLO HAWK geologic setting and relative displacements is included here. For a full description see the summary by Short and Kennedy (1978). Both MIGHTY EPIC and DIABLO HAWK were sited at the Nevada Test Site in the U 12n.10 tunnel system beneath Rainier Mesa. The tunnel system, shown in plan view in Figure 5, is approximately 400 m beneath the Mesa surface and extends horizontally into the shot area from the portal in the side of the mesa.
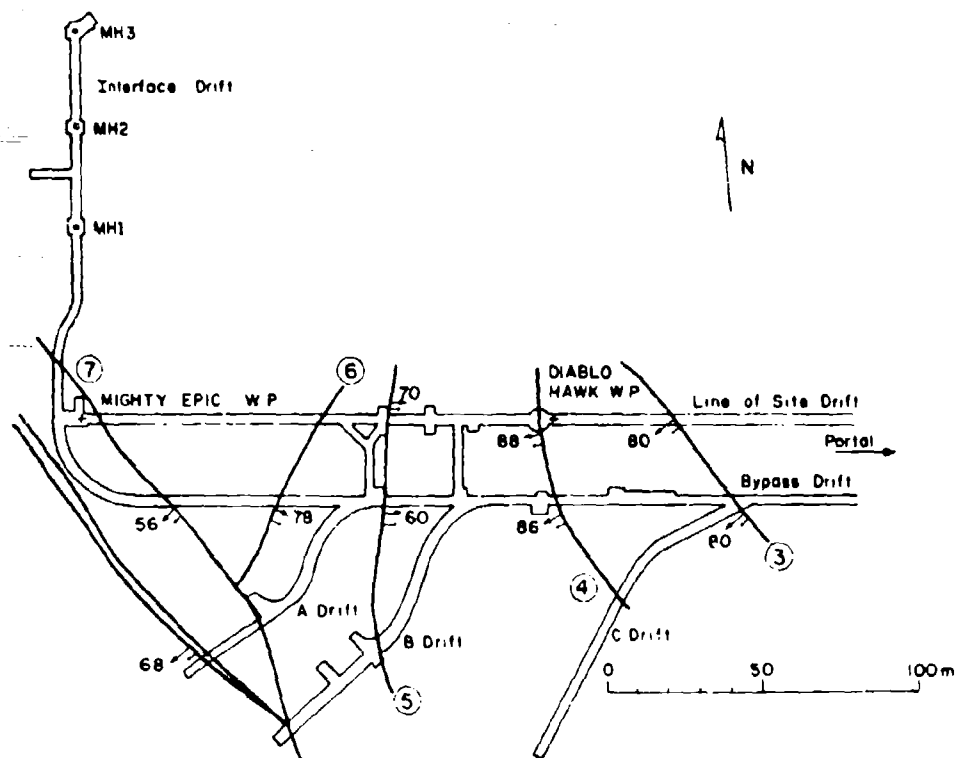
Figure 5. MIGHTY EPIC tunnel system and major faults (from Short and Kennedy 1978).
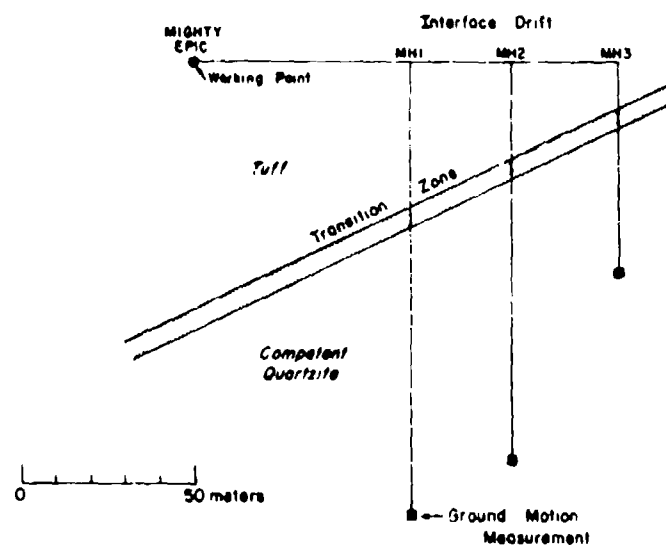

Figure 6. Schematic section - tuff/quartzite interface (from Short and Kennedy 1978).

6

The two shot locations (or working points) were about 152 m apart, lying in the Main, or Line of Site (LOS) drift. MIGHTY EPIC was fired in 1976 and DIABLO HAWK in 1978. The A, B and C drifts contained experimental structures of various configurations and hardnesses. Additional tunneling and experiments were added prior to DIABLO HAWK. The interface drift provided access to the tuff/quartzite interface which dipped south beneath the drift and the working point. The top of the competent quartzite, as shown schematically in Figure 6, lay approximately 19 m below the floor of the drift at hole MH3, 46 m below the floor at hole MH1, and 79 m below the working point.

The material properties of the tuff in the area of the drifts containing the structures are reported by Butters (1976). The tuff had an average porosity of 31%, a density of 1.95 g/cm^3, and an unconfined compressive strength of 195 bars. Ultrasonic laboratory p and s wave velocities averaged 3140 and 1580 m/s respectively. Tabulated data presented by Short and Kennedy (1978) indicate that average tuff properties in other areas generally vary less than 10% from these values.

Figure 5 shows a plan view of the major faults in the area of the MIGHTY EPIC works. Fault numbers 3 through 8 are throughgoing and can be extrapolated to faults or lineations on the surface of the mesa. All these major faults are normal faults, and most strike north to northwest, dip steeply toward the west, and exhibit small displacements. The faults are very tight, with the fault zones generally less than 0.01 m thick. Short and Kennedy (1978) report that the faults themselves, as well as the surrounding rock, have very low permeability—usually well below a millidarcy. In addition to the faults, there are also numerous bedding planes within the tuff. These have a shallow dip (on the order of 15°) toward the south-southeast.

In situ stresses beneath Rainier Mesa appear to vary considerably in magnitude and orientation. Figure 7 is a plot of maximum and minimum horizontal stress from seven locations beneath the mesa, obtained using an overcoring technique (Ellis 1976). According to Short and Kennedy (1978), the maximum horizontal stress averaged 70 bars, the minimum horizontal stress averaged 33 bars, and the vertical stress averaged 63 bars, which agrees with the overburden stress at the depth of the measurements. The inclination of the actual principal stresses varies from site to site. The maximum horizontal stresses are oriented toward the northeast and the minimum horizontal stresses toward the northwest.
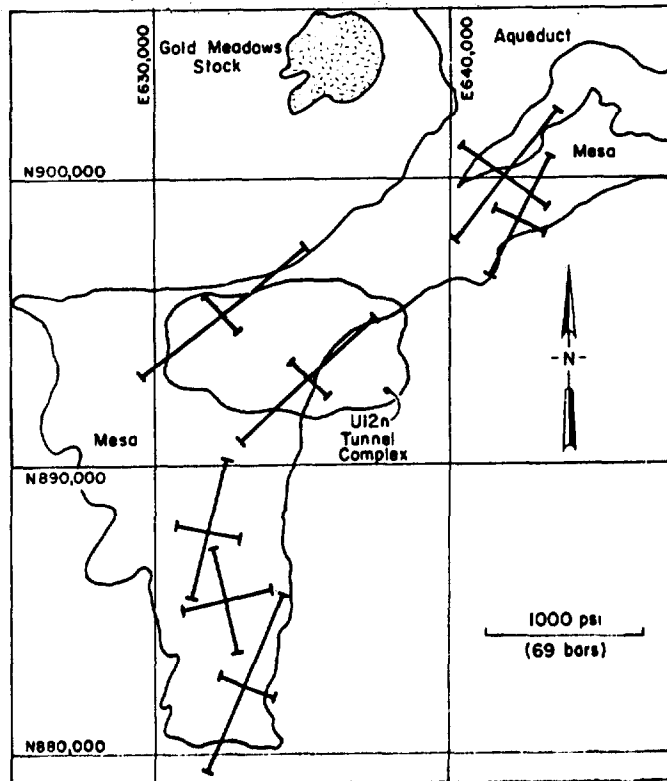

Figure 7. Secondary principal stresses in horizontal plane for seven locations in Rainier Mesa (from Ellis 1976).

7

For all MIGHTY EPIC and DIABLO HAWK stress calculations in this study, the approximation of in situ stresses shown in Figure 8 was used. The principal stresses were assumed to have vertical and horizontal orientations. A vertical stress of 80 bars was assumed. This was approximately equal to the overburden stress at the depth of the shots. The maximum horizontal principal stress (80 bars) was assumed equal to the vertical stress and oriented N 45° E. The minimum horizontal principal stress (40 bars) was assumed equal to half the maximum and was oriented N 45° W.

The relative displacements documented for MIGHTY EPIC are shown in the plan view of Figure 9 and are listed in Table 2 (both after Kipp and Kennedy 1978). All displacements, except the fault near the end of the Interface drift, were similar to those observed during the DIHEST events in that relative displacement was always relative to the foot wall, as shown schematically in Figure 10. It appears likely that upward vertical motion along the tuff/quartz interface beneath the interface fault resulted in displacement in the normal mode along this fault.

Relative displacements along the interface, as determined by a post-test magnetometer survey, were approximately 2.1 m outward from the working point and upward at the 61-m range of hole MH1 (see Fig. 6), dropping to about 0.8 m at the 122-m range of hole MH3. Both the remainder of the fault displacements and the bedding plane displacement between tunnel bed subunits 3BC and 3D had reverse dip slip. The magnitude of displacement of the small fault between faults 5 and 6 which intersected the SRI ministructure could not be determined. Structural deformation indicated that the fault moved with reverse dip slip and left lateral strike components. The strike
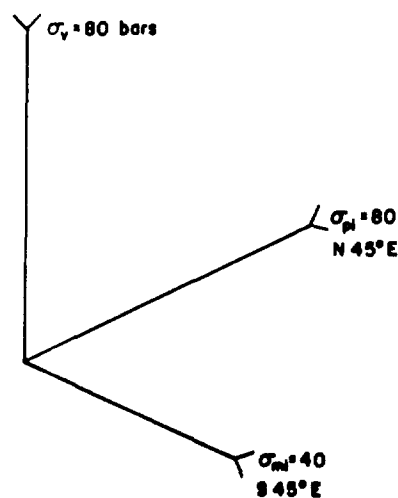

Figure 8. Shot level approximation of principal in situ stresses.

slip components of the 3BC-3D bedding plane slip and the fault near fault 6 in the LOS drift could not be determined.

The displacement indicated in Figure 9 at the intersection of fault 6 with the Bypass drift is somewhat confusing. According to Kipp and Kennedy (1978), the fault at this location is actually a zone of multiple discontinuities rather than a well defined slip surface. Relative displacement was measured only in the right rib (or north side) of the drift. This apparently consisted of an 0.8-m compression across the fault zone and a 0.6-m increase in drift diameter. There is a possibility that displacement in this area was rotational. Because of these irregularities, this motion was not listed in Table 2, nor is it included in the MIGHTY EPIC analysis.

Shear stress analysis

Analysis of the MIGHTY EPIC relative displacements was separated into two parts. First, the approximate peak shear stresses acting at the location of each displacement were analyzed in an attempt to define the properties governing the in situ shear strengths of the faults. Second, the magnitudes of displacement were analyzed to devise a semi-empirical model for predicting fault displacements at depth. The first part of the analysis resulted in a method for predicting both the location and direction of relative displacements, the second resulted in a method for predicting their magnitude.

The prediction of relative displacement locations and directions is based on the calculation of the peak shear and normal stresses acting on a particular fault, at a particular location on that fault. The peak shear stress is then compared to the critical shear stress given by the Mohr-Coulomb failure criterion as

$$\tau_c = \tau_0 + \sigma_n \tan \phi \qquad (5)$$

where τ_c is the critical shear stress, which is equivalent to the shear strength of the fault under the conditions of in situ stress and dynamic loading, τ_0 is a measure of the cohesion and/or mechanical interlocking of the fault under zero normal stress, σ_n is

Table 2. Observed MIGHTY EPIC relative displacements.

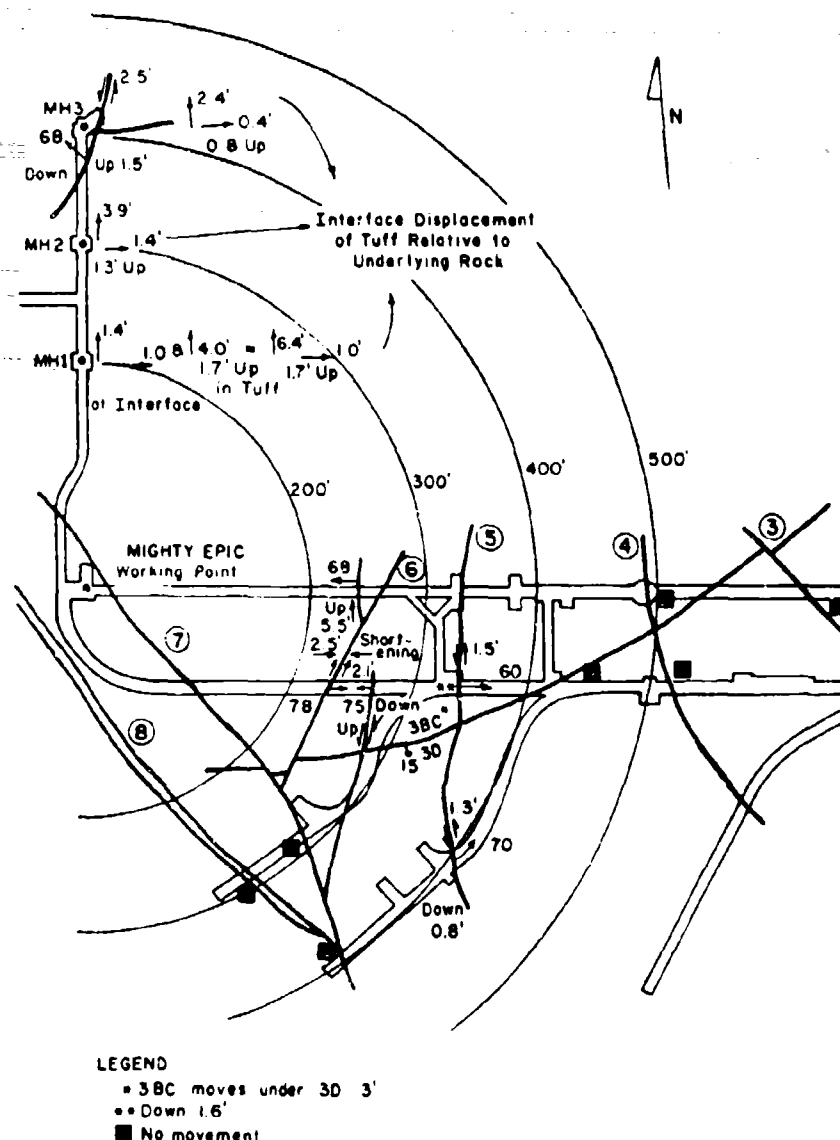| Slip location	Displacement (m)		
	Strike slip	Dip slip	Total
Fault 5 B drift	0.40	0.24	0.46
Fault 5 Bypass drift	0.45	0.49	0.67
Fault near fault 6—LOS drift	-	1.68	>1.68
3B/3D bedding plane	—	0.91	>0.91
Fault through SRI ministructure	>0	>0	>0
Fault through Interface drift	≈0.76	≈0.46	≈0.88

Figure 9. Block motion resulting from the MIGHTY EPIC event (from Short and
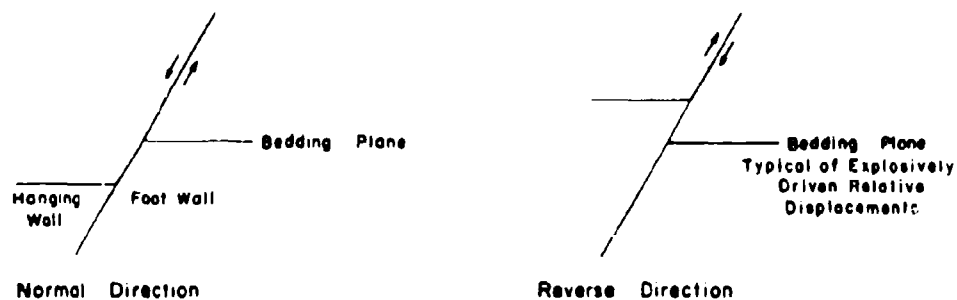Kennedy 1978).

Figure 10. Schematic section view—normal and reverse faults.

9

the peak normal stress acting on the fault, and ϕ is the friction angle of the fault. If the peak shear stress exceeds the critical shear stress τ_c it is assumed that motion along the fault plane will result. The direction of slip would be expected to follow the direction of the peak shear stress vector. The magnitude of peak shear is given by

$$\tau_r = (\tau_s^2 + \tau_d^2)^{1/2} \tag{6}$$

where τ_s and τ_d are the peak shear stresses in the direction of the fault strike and dip, respectively, and τ_r is the resultant of these two shear vectors—with a magnitude equal to their Pythagorean sum and a direction governed by their signs.

The expressions for the peak normal stress and peak dip and strike shear stresses were derived by using the schematic of the slip plane shown in Figure 11 and notation from Timoshenko and Goodier (1970). The slip plane, represented by the plane abc, is oriented with respect to the orthogonal axes x, y and z, along which the peak principal stresses act as shown. For the geometry of the MIGHTY EPIC and DIABLO HAWK experiments, with the fault documentation locations at the same level as the shot point and the principal in situ stresses oriented horizontally and vertically as depicted in Figure 8, the peak combined principal stresses will also act horizontally and vertically. Thus, the angle θ is taken as the angle between the slip plane strike and the maximum peak horizontal principal stress σ_p which acts in the x direction. The minimum peak horizontal principal stress σ_m acts in the y direction and the vertical principal stress σ_v acts in the z direction. The angle β is the slip plane dip. Line-on is perpendicular to the slip plane at point n. Let X, Y and Z be components of stress on plane abc acting in the principal stress orientation x, y and z, respectively, and let the area of abc be equal to A.

To satisfy equilibrium, the sum of forces in each of the x, y and z directions must equal zero. The sum of forces in the x direction is expressed as

$$\Sigma F_x = XA - A \cos (aon) \sigma_p = 0 \tag{7}$$

where $A \cos (aon)$ equals the area of plane obc. Solving for X yields

$$X = \sigma_p \cos (aon) \tag{8}$$

and a similar procedure for forces in the y and z directions yields

$$Y = \sigma_m \cos (bon) \tag{9}$$

and

$$Z = \sigma_v \cos (con) \tag{10}$$

Using the stress components X, Y and Z, the shear stress in the direction of the slip plane strike τ_s, the shear stress in the direction of the slip plane dip τ_d, and the normal stress on the slip plane σ_n can be obtained as shown in the horizontal and vertical sections through the slip plane in Figure 12. The strike shear, defined as positive when acting on the slip plane in the negative x direction, is given by

$$\tau_s = X \cos \theta - Y \sin \theta \tag{11}$$

Combining with eq 8 and 9 yields

$$\tau_s = \sigma_p \cos (aon) \cos \theta - \sigma_m \cos (bon) \sin \theta \tag{12}$$

The dip shear, defined as positive when acting upward on the slip plane, is given by

$$\tau_d = X \sin \theta \cos \beta + Y \cos \beta - Z \sin \beta \tag{13}$$

Combining with eq 8-10 yields

$$\tau_d = \sigma_p \cos (aon) \sin \theta \cos \beta + \sigma_m \cos (bon) \cos \theta \cos \beta - \sigma_v \cos (con) \sin \beta \tag{14}$$

The normal stress on the slip plane, defined as positive when acting toward the origin, is given by

$$\sigma_n = X \cos (aon) + Y \cos (bon) + Z \cos (con) \tag{15}$$

which combined with eq 8-10 yields

$$\sigma_n = \sigma_p \cos^2 (aon) + \sigma_m \cos^2 (bon) + \sigma_z \cos^2 (con) \tag{16}$$

The cosines of aon, bon and con must be expressed in terms of β and θ. From Figure 11:

$$\cos (aon) = \frac{on}{oa} \tag{17}$$

where

$$on = om \sin \beta \tag{18}$$

and

$$om = oa \sin \theta \tag{19}$$

10
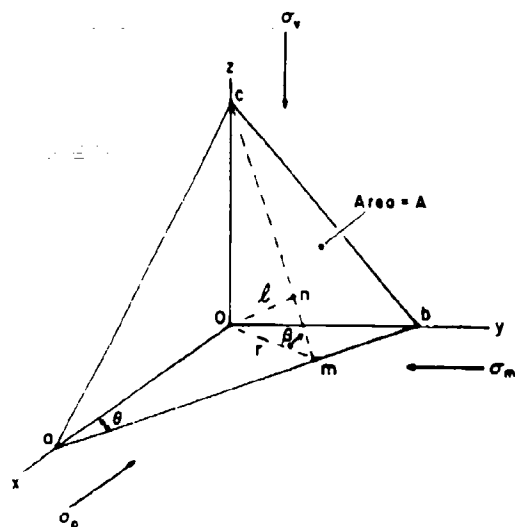
Figure 11. Geometry of slip plane abc.
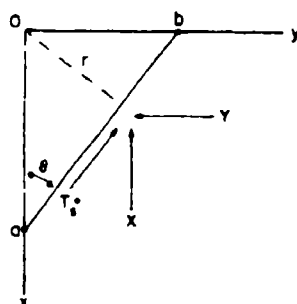
Slip plane--horizontal section
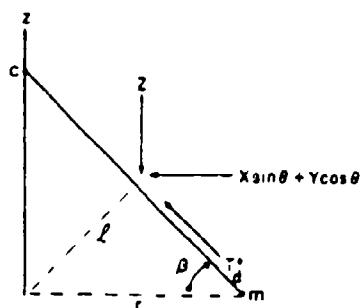
Slip plane--vertical section

Figure 12. Sections through slip plane abc.

Substituting eq 18 and 19 into eq 17 yields

$$\cos(aon) = \sin\theta \sin\beta \qquad (20)$$

Similarly, it can be shown that

$$\cos(bon) = \cos\theta \sin\beta \qquad (21)$$

and by inspection,

$$\cos(con) = \cos\beta \qquad (22)$$

Substituting eq 20-22 into eq 12, 14 and 16 and manipulating them yields the following expressions for the shear and normal stresses on the slip plane as functions of the peak principal stresses and the fault dip and strike:

$$\tau_s = \frac{\sigma_p - \sigma_m}{2} \ (\sin 2\theta \sin\beta) \qquad (23)$$

$$\tau_d = (\sigma_p \sin^2\theta - \sigma_m \cos^2\theta - \sigma_v) \frac{\sin 2\beta}{2} \qquad (24)$$

$$\sigma_n = \sigma_p \sin^2\theta \sin^2\beta + \sigma_m \cos^2\theta \sin^2\beta + \sigma_v \cos^2\beta \qquad (25)$$

In order to apply the above equations at a particular location along any fault or bedding plane, the magnitude and orientation of the peak principal stresses must be established. These are obtained by superimposing an approximation of the critical principal dynamic stresses at the location of interest on the in situ stress approximation shown in Figure 8. The critical dynamic state of stress is assumed to occur shortly after passage of the stress front. The peak principal dynamic stress is radial in compression and is approximated by

$$\sigma_r = \rho c v_t \qquad (26)$$

where ρ is the mass density of the rock, c the compressive wave speed, and v_t the peak radial particle velocity at the location of interest on the slip plane. Figure 13 is a logarithmic plot of peak particle velocity and stress, scaled by the cube root of yield, used to determine peak radial stresses for both MIGHTY EPIC and DIABLO HAWK (from Short and Kennedy 1978). This plot is a fit to past data in this rock type and it proved to be a good fit to the MIGHTY EPIC data. A compression wave speed of 2590 m/s and density of 1.96 g/cm³ were used to convert the peak particle velocity to stress. The minor dynamic

11

Figure 13. *MIGHTY EPIC-DIABLO HAWK peak radial stress and particle velocity approximation (after Short and Kennedy 1978).*

Figure 14. Normalized stresses from a spherically expanding wave in an elastic medium (after Selberg 1952 and Rinehart 1975).

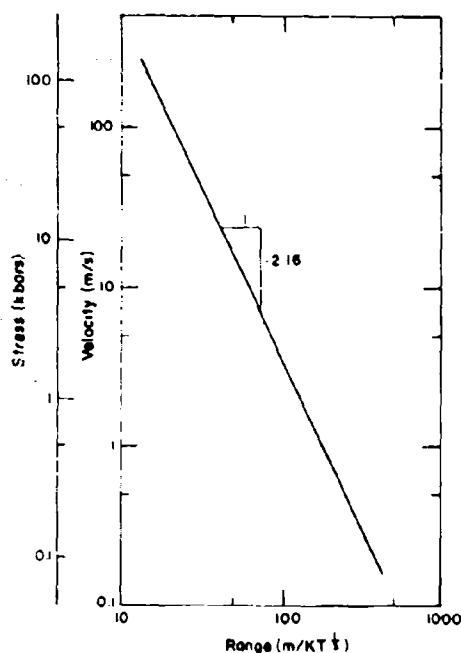principal stresses are in the tangential direction. Unfortunately, according to Bass (pers. comm.), there are no credible tangential stress data upon which to base approximations of the critical minor principal stresses. Thus, the elastic solution for a spherically expanding stress wave from a spherical cavity was used as a guide in picking the critical minor stresses. Selberg (1951) and Rinehart (1975) give solutions for a Heaviside pressure pulse (nondecaying step input), applied to a sphere of radius r_0 in an infinite elastic medium having a compression wave speed c and Poisson's ratio of 0.25. Graphs of radial stress, tangential stress and maximum shear stress for ranges of r_0, $2r_0$ and infinity are shown in Figure 14 (from Selberg 1951). For comparison, the curves are normalized by multiplying the amplitudes by r/r_0 and by defining time t' as

$$t' = \frac{ct}{r_0} - \frac{r - r_0}{r_0} \qquad (27)$$

where t is real time.

At the wave front, both radial and tangential stresses are compressive. This is followed by a rapid reversal of tangential stress into tension. At a range of $2r_0$, which most nearly corresponds to the ranges of interest in the underground tests, the maximum shear stress remains nearly constant during the course of

this reversal, while at smaller ranges it increases and at greater ranges it decreases. Based on these observations, a logical approximation of the critical dynamic stress state (i.e., that state producing the highest components of shear stress) is radial stress at its peak value. This peak value of radial stress occurs shortly behind the initial arrival of the compression wave and, with tangential stress at zero, would represent the rapid reversal in tangential stress. Tensile stresses are not allowed since it is believed that large masses of in situ rock can support little or no tensile stress because of the many zones of weakness which are always present. In actuality this assumption of critical stresses is probably conservative since the radial stress should begin decreasing by the time tangential stress drops to zero.

With the critical dynamic stress state now defined, it must be superimposed on the in situ stresses to obtain the magnitude and orientation of the principal stresses acting on the slip plane at the point of interest. For both MIGHTY EPIC and DIABLO HAWK,

12

the displacement documentation locations are at the same elevation as the working point. Therefore, the dynamic radial stress has no component in the vertical direction and will interact only with the horizontal components of the principal stress approximation shown in Figure 8. A schematic plan view of this interaction is shown in Figure 15. Angle α is defined as the angle between the direction of propagation of the radial stress σ_r from the working point and the normal to the plane on which the principal stress acts. It is measured counterclockwise. Mohr circles are used to depict the superposition of stresses in Figure 16. The first portion of the figure shows the dynamic critical principal stresses σ_r and the assumed critical tangential stress of zero. Diameter ab represents the principal planes on which the in situ stresses act. The normal component of dynamic stress acting on the major in situ principal plane σ_{rp} is given by

Figure 15. *Interaction between dynamic and in situ principal stresses.*

Figure 16. Mohr's circle representation--summation of horizontal stresses.

13

$$\sigma_{rp} = \frac{\sigma_r}{2} \ (1 + \cos 2\alpha) \qquad (28)$$

and the normal component of dynamic stress acting on the minor in situ principal plane σ_{rm} is given by
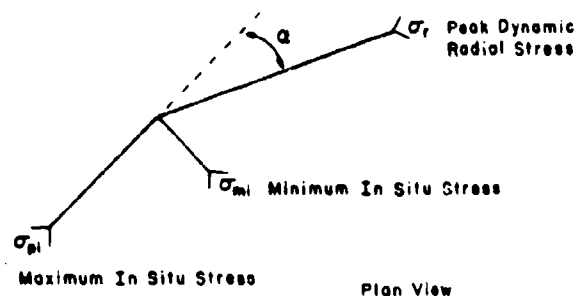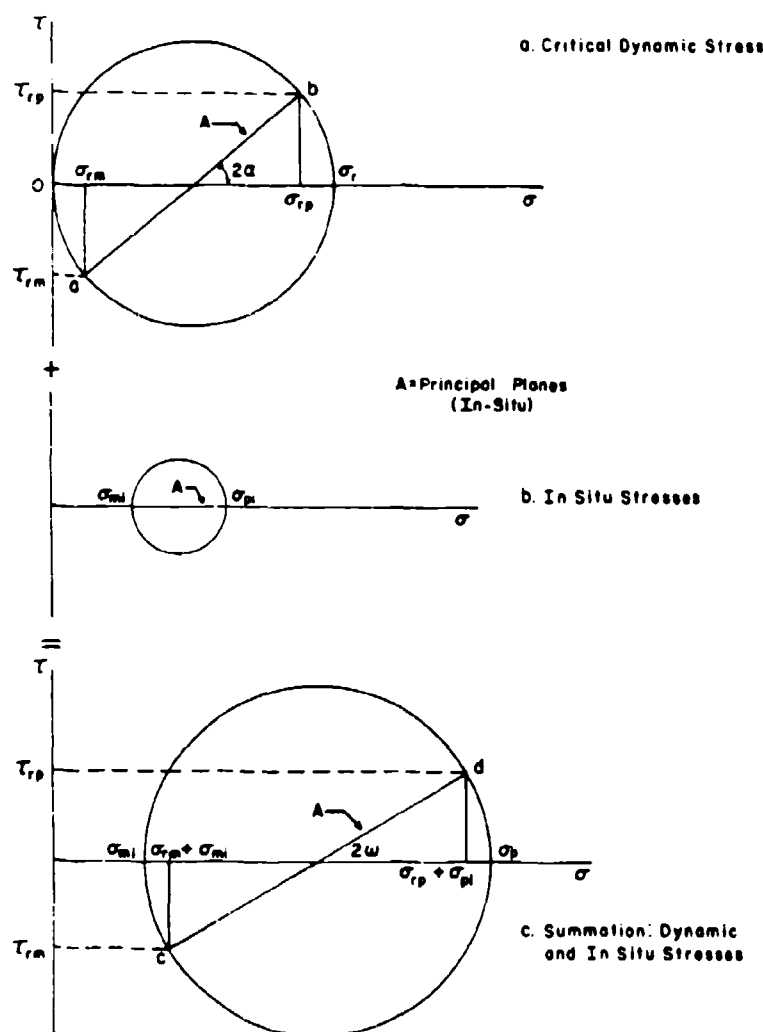
$$\sigma_{rm} = \frac{\sigma_r}{2} \ (1 - \cos 2\alpha) \qquad (29)$$

The shear component of dynamic stress acting on the major in situ principal plane τ_{rp} is given by

$$\tau_{rp} = \frac{\sigma_r}{2} \ \sin 2\alpha \qquad (30)$$

and the dynamic shear component acting on the minor plane τ_{rm} is given by

$$\tau_{rm} = -\frac{\sigma_r}{2} \ \sin 2\alpha \qquad (31)$$

The in situ stresses on the in situ principal planes are represented in Figure 16b. In this instance, of course, there are no shear components and the principal planes lie along the horizontal axis. Figure 16c represents the sum of the dynamic and in situ horizontal stresses and defines a new set of principal stresses resulting from a combination of the two. The in situ principal planes lie along the diameter cd. The normal stress on the major principal plane is now $\sigma_{rp} + \sigma_{pi}$, while the shear component remains equal to τ_{rp}. Likewise, the normal component on the minor plane remains τ_{rm}. The planes upon which the new combined principal stresses act are oriented at the angle ω with respect to the original in situ principal planes. Application of geometry and algebraic manipulation yields an expression for ω of

$$\omega = \frac{\cot^{-1} \ [\cot 2\alpha + \frac{\sigma_{pi} - \sigma_{mi}}{\sigma_r \sin 2\alpha}]}{2} \qquad (32)$$

Also, an expression for the major and minor combined principal stresses, σ_p and σ_m respectively, can be derived:

$$\sigma_{p}, \sigma_m = \frac{\sigma_r + \sigma_{mi} + \sigma_{pi}}{2} \pm \left[\frac{\sigma_r^2}{4} + \frac{\sigma_r \cos 2\alpha \ (\sigma_{pi} - \sigma_{mi})}{2} + \left(\frac{\sigma_{pi} - \sigma_{mi}}{2} \right)^2 \right]^{\frac{1}{2}} \qquad (33)$$

The major principal stress is obtained by adding the expression in brackets and the minor principal stress is obtained by subtracting this expression. Figure 17 is a schematic view of the relationship among the combined principal stresses, the original in situ stresses and the dynamic stress.

The combined principal stresses can then be used in eq 23-25 to define the peak normal and shear stresses on any potential slip plane. The angle θ between the major principal stress and the strike of the slip plane is determined by finding the orientation of the principal stresses using eq 32. The peak strike and dip shear stress are combined using eq 6 to obtain the resultant peak shear stress on the slip plane. Peak resultant shear stresses were thus obtained at each MIGHTY EPIC relative displacement location listed in Table 2. Since failure occurred in each of these instances, it is assumed that the resultant shear stress exceeded the shear strength given by the Mohr-Coulomb failure criterion in eq 5. This is expressed as

$$\tau_r > \tau_0 + \sigma_n \tan\phi \qquad (34)$$

Using an approximation for the cohesion τ_0 obtained from an extrapolation of the DIHEST results, the maximum friction angle which would permit motion at each slip plane location on MIGHTY EPIC was calculated.

The cohesion approximation is derived from a set of assumptions based on the observation (Blouin 1980) that relative displacements were never observed beyond a range of three crater radii during the DIHEST series. Taking this observation as a generalization, the cohesion can then be calculated for a surface burst geometry. As shown in the schematic diagram of Figure 18, the peak radial stress is calculated at a range of three crater radii from a surface burst. This is assumed to be the maximum range at which slip will occur. As in the case of the contained burst, the critical tangential stress is taken as zero. In addition, it is assumed that near-surface in situ stresses are negligible. Thus the peak principal stresses of zero and σ_r, as shown on the Mohr diagram of Figure 19, will act on any potential slip planes at that range. Slip will occur, as shown, if a slip plane is oriented such that its failure envelope is just tangent to the Mohr circle. This condition will be satisfied only by planes oriented at an angle of $45° \pm \phi/2$ to the radial stress vector. For any such plane, the conditions for tangency to the circle are governed by a combination of ϕ and τ_0. From geometry, the equation for cohesion as a function of peak radial stress and friction angle can be expressed as

$$\tau_0 = \frac{\sigma_r \ (1 - \sin\phi)}{2 \cos\phi} \qquad (35)$$

14
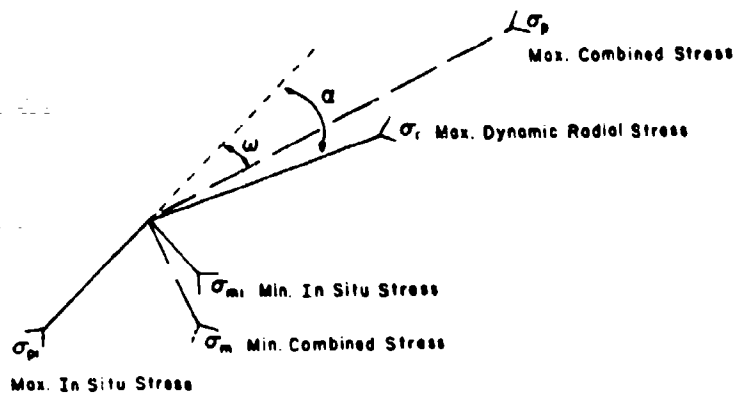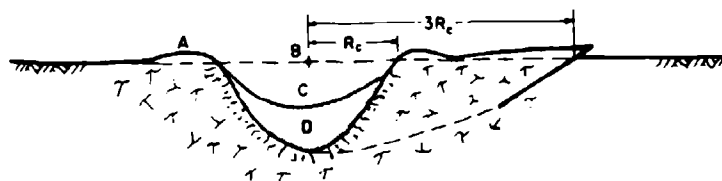
Figure 17. Schematic plan view—combined horizontal principal stresses.

A - Lip
B - Shot Point
C - Apparent Crater
D - True Crater
▨ - Rupture Zone
▭ - Fallback
▦ - Displaced Block

Figure 18. Schematic section view—hypothesized limit for surface burst relative displacement.
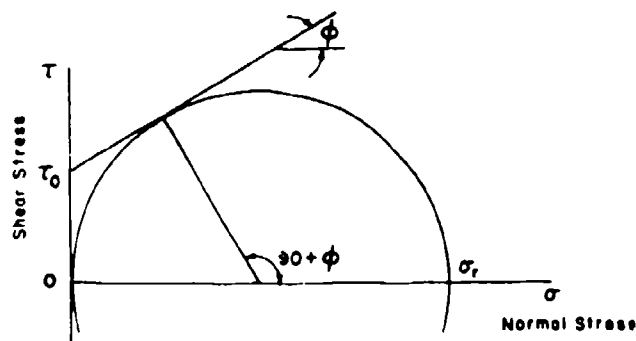

Figure 19. Assumed near-surface critical stress state.

15

The value of radial stress at a range of three crater radii is, of course, dependent on the surface-burst crater radius which, according to Crawford et al. (1974), is subject to a great deal of uncertainty, particularly in the case of high yield nuclear bursts. This uncertainty results in peculiar variations in cohesion as a function of yield. The prediction relationships recommended by Crawford et al. (1974) are based on the high yield nuclear tests conducted at Eniwetok and Bikini atolls which produced abnormally broad and shallow craters as compared to those from low yield nuclear and HE events (Ristvet et al. 1978). It is not known whether this abnormality was geology-dependent or somehow related to the high yields. However, it has the effect of making the cohesion according to eq 35 yield-dependent.

Figure 20 is a plot of cohesion as a function of yield for high energy nuclear and HE surface bursts. It is based on the prediction techniques for dry, soft rock outlined in Crawford et al. (1974) and in eq 35. The plot includes a band of friction angles from 20 to 40°. This encompasses most values presented in the literature. The discontinuity between the high explosive and nuclear portions of the plot near the 1-Kton level is due to several factors. First, the cratering efficiency of the HE is about 20 times that of the nuclear, and second, the equivalent yield coupling factor for half-buried HE is about 20%, versus only 4% for the nuclear surface burst. Using the radial stress given in Figure 13, i.e., no effect of the free surface is included except the reduction in coupling efficiency already noted, the band of cohesion ranges from about 9 to 14 bars for a 10-Mton nuclear surface burst. This increases to 45 to 70 bars for a 1-Kton nuclear burst, but remains constant with yield at between 11 and 18 bars for the HE bursts. For comparison, the calculated cohesion from the ROCKTEST II-DIHEST displacements listed in Table 1 ranged from 35 to 53 bars, which tends to agree with the low yield nuclear portion of the plot. It should be remembered, however, that all significant DIHEST related displacements occurred along joints, rather than faults, which would tend to have a higher cohesion because the small interlocking asperities have not been sheared off by previous movement. For this reason, as well as the desire to keep the assumed MIGHTY EPIC cohesion on the conservative side, a cohesion of 10 bars, which lies on the low side of the calculated values, was used in the MIGHTY EPIC analysis and for the DIABLO HAWK predictions.

This completes the engineering approximations and assumptions necessary to evaluate the shear strength parameters at each displacement location on MIGHTY EPIC. In summary, the Mohr–Coulomb failure criterion is used to obtain the upper limit of the friction angle at each location using a rearrangement of eq 34 given by

$$\phi \leq \tan^{-1}\left(\frac{\tau_r - \tau_0}{\sigma_n}\right) \qquad (36)$$

According to this assumption, the in situ friction angle must have been less than or equal to the value calculated at each location for slip to have occurred. A cohesion of 10 bars was assumed, based on the extrapolation of the outlined DIHEST experience. The values of the peak normal and resultant shear stresses acting at each location were obtained from eq 6 and 23–25. The peak principal stresses used in these equations were calculated by superimposing the critical dynamic principal stresses on the in situ stress approximation of Figure 8. The parameters used at each MIGHTY EPIC displacement location are listed in Table 3. Because they are classified, the dynamic stresses and peak combined principal stresses are not included in the table. The computed upper limits of the friction angle at each displacement location, using the assumed value for cohesion of 10 bars, are listed. These ranged from 61.5° at the 3BC/3D bedding plane to 29.0° at the intersection of fault 5 with the Bypass drift. Again, these are the highest friction angle values which would have allowed slip at each location. Had the values been less, slip would still have occurred. Had values been greater than those listed, slip would not have occurred.

The direction of the resultant shear vector τ_r is denoted in Table 3 by the angle γ. This angle is measured in the plane of the fault, viewing the fault from the working point side. It is the angle between the fault strike and the resultant shear vector and is given by

$$\gamma = \tan^{-1}\left(\frac{\tau_d}{\tau_s}\right) \qquad (37)$$

The sign convention is for positive values of γ to have a vertical component of motion. Left lateral motion means that the fault block opposite the working point block should move to the left, relative to the working point block. Right lateral motion infers relative movement to the right. As shown in Table 3, the directions of motion measured on MIGHTY EPIC generally agree well with the calculated directions of the peak shear stress vectors. The poorest agreement is the 38° discrepancy on the fault which intersects the Interface drift. This discrepancy can be explained by the fact that the working point block must have an upward component of motion as it moves outward along the underlying, upward-sloping quartzite interface shown in Figure 6. Thus, instead of reverse thrust motion on the interface fault, which is typical
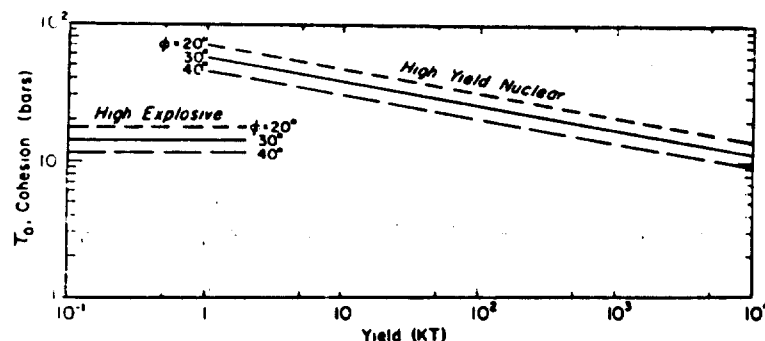
16

Figure 20. Cohesion to limit relative displacement to three crater radii.

Table 3. MIGHTY EPIC displacement parameters.

Location	Range (m)	Strike	Dip	Direction from W.P.	ϕ	γ predicted	γ measured	$\Delta\gamma$
Fault 5 B drift	122	N11°E	70°SE	S42°E	≤45.5°	-24.2°RL*	-31.6°RL	7.4°
Fault 5 Bypass drift	103	N13°E	60°SE	S63°E	≤29.0°	-64.7°RL	-46.9°RL	17.8°
Fault near fault 6— LOS drift	72	N11°E	55°NW	S79°E	≤33.2°	89.1°LL	N.D.	—
3BC/3D bedding plane	89	N82°E	15°SE	S44°E	≤61.5°	-53.6°LL	N.D.	—
Fault through SRI mini-structure	86	N27°E	60°NW	S46°E	≤31.7°	57.8°RL	N.D.	—
Fault through Interface drift	116	N34°E	68°NW	N10°E	≤57.2°	- 6.7°RL	31.0°RL	37.7°

* RL is right lateral displacement, LL is left lateral displacement.

of all other MIGHTY EPIC and DIHEST data, motion is in the normal mode.

Displacement analysis

It was shown in the DIHEST analysis section that the upper bound of the magnitude of displacements associated with the DIHEST shots was given by a conservation of block energy equation (eq 4) where the block has an initial kinetic energy proportional to the square of the peak particle velocity at the range of slip. In instances where geometric or air overpressure constraints did not inhibit block motion, maximum differential displacements closely matched those calculated using eq 4. This approach was modified to account for deep burial, with parameters adjusted to yield good agreement between the MIGHTY EPIC displacements and the calculated displacements. This semi-empirical technique was then used to predict the DIABLO HAWK block motion magnitudes.

The extrapolation from surface relative displacements driven by near-surface cratering bursts to subsurface displacements driven by contained bursts is complicated by: 1) the subsurface displacement blocks are defined only at their intersection with post-test excavations, and 2) credible ground motion and stress time histories directly adjacent to planes of slip do not exist. The first complication makes it impossible

to estimate the total kinetic energy of a displaced block. The second makes it difficult to assess the normal stress distribution on a fault surface during displacement, which is, of course, the key to determining the frictional energy absorption.

In order to overcome the first difficulty, an increment of the block mass is used which acts on an increment of the fault plane as shown in Figure 21. This mass increment is assumed to extend radially from the cavity wall formed by the detonation to the slip plane. Its mass m_i is given by

$$m_i = \frac{\rho \pi \ell_0^2 (r^3 - r_c^3)}{3r^2} \qquad (38)$$

where ρ is the mass density of the rock, ℓ_0 the radius of the increment at the slip plane, r the range from the working point to the slip plane, and r_c the cavity radius formed by the explosion. The area of the increment, normal to the radius, from the working point to the slip plane, given by $\pi \ell_0^2$, is taken as unity. Equation 3 can now be rewritten in a form suitable to the underground case as

$$\tfrac{1}{2} m_i v_m^2 = \mu f_g \int_0^\delta \sigma_n (x) \, dx + m_i g \delta_v \qquad (39)$$

17

where the kinetic block energy, $\frac{1}{2}m_i v_r^2$, equals half the increment mass multiplied by the square of the peak radial velocity at the slip plane. The first group of terms to the right of the equal sign represents the energy dissipated by friction. This is the integral of the normal stress $\sigma_n(x)$ acting on the plane, which is assumed to vary with displacement in the x direction (taken as the direction of the principal shear stress), multiplied by the coefficient of friction μ, and a term f_g which equals the area of the slip plane intercepted by the mass increment. The area f_g is given by

$$f_g = \frac{1}{\sin\eta \sin\beta} \qquad (40)$$

where η is the angle between the radial velocity vector and the slip plane strike and β, the slip plane dip. Thus the entire integral term represents a varying friction force integrated over the length of displacement δ. The final term in eq 39 is simply the change in potential energy due to vertical translation of the mass increment. By defining the vertical component of displacement δ_v as a function of the total displacement and slip plane orientation, and by approximating the integral terms, the total displacement δ can be obtained.

By approximating the integral term the second complication of the contained burst extrapolation, that of lack of appropriate stress time histories, is circumvented. Three different approximations of the integral term were used to make post-test "predictions" of MIGHTY EPIC displacement magnitudes. The model giving the best overall fit to the displace-

ment data was then used to make the DIABLO HAWK predictions. The three approximations are shown in Figure 22. In all cases the normal stress is initially assumed to equal the peak normal stress σ_n of eq 25, computed from superimposing the peak dynamic normal stress on the in situ normal stress. The normal stress at the conclusion of slip is, in all cases, assumed equal to the pretest in situ normal stress σ_{ni} on the slip plane. It is calculated using eq 25 with σ_{pi} and σ_{mi} substituted for σ_p and σ_m, respectively, and with θ computed as the angle between the strike of the slip plane and the direction of σ_{pi}. The differences between the three models are in the rates of normal stress dissipation. Model 1 assumes that the dynamic component is dissipated linearly over the entire displacement δ. Model 2 assumes that the dissipation occurs linearly in only half the total displacement, with the remaining displacement occurring under the in situ normal stress. Model 3 assumes a linear dissipation which is independent of the total displacement. Trial and error showed that a displacement of 0.3 m gave the most reasonable fit to the MIGHTY EPIC data. Again, the remaining slip was assumed to occur under the in situ normal stress. The integral in eq 39 was thus defined as the area within each of the three normal stress distributions shown in Figure 22. It should be noted that none of the three models is meant to rigorously represent the actual normal stress attenuation on the plane of weakness. They are simple representations of possible attenuation mechanisms and provide a simple means of evaluating the integral in eq 39.

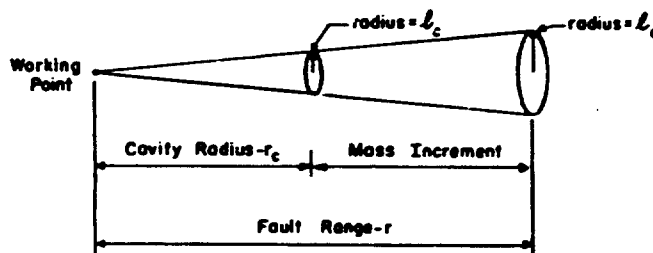The vertical component of relative displacement δ_v is given by
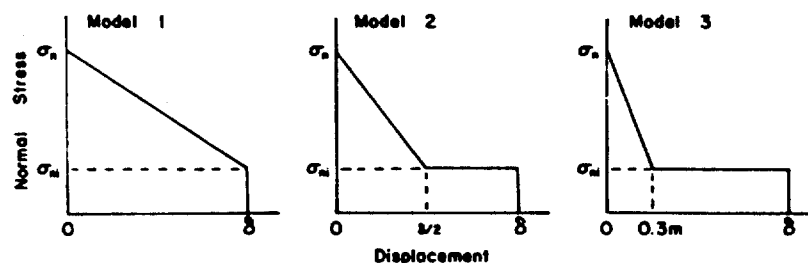

Figure 21. Depiction of mass increment.

Figure 22. Normal stress dissipation models.

18

$$\delta_v = \delta_d \sin\beta \qquad (41)$$

where δ_d is the dip component of displacement. Assuming displacement occurs in the direction of the peak resultant shear stress, δ_d can then be defined as

$$\delta_d = \delta \sin\gamma \qquad (42)$$

where γ is the angle between the resultant shear stress and the slip plane strike shown in Figure 12. By inspection

$$\sin\gamma = \frac{\tau_d}{\tau_r} \qquad (43)$$

Combining eq 41–43 gives an expression for the vertical component of displacement as a function of the dip shear stress, resultant shear stress and slip plane dip:

$$\delta_v = \delta \frac{\tau_d}{\tau_r} \sin\beta \qquad (44)$$

Substituting the areas of each of the normal stress dissipation models for the integral in eq 39 and substituting eq 44 for δ_v gives solutions of total displacement for each of the dissipation models. The solution for model 1 in which the dynamic normal stress is linearly dissipated over the entire displacement is given by

$$\delta = \frac{m_i v_r^2}{\mu f_g (\sigma_n + \sigma_{ni}) + 2m_i g \dfrac{\tau_d}{\tau_r} \sin\beta} \qquad (45)$$

The solution for model 2 in which dynamic normal stress is dissipated over half the total displacement is given by

$$\delta = \frac{m_i v_r^2}{\tfrac{1}{2}\mu f_g (\sigma_n + 3\sigma_{ni}) + 2m_i g \dfrac{\tau_d}{\tau_r} \sin\beta} \qquad (46)$$

The solution for model 3 in which dynamic normal stress is dissipated over 0.3 m displacement is given by

$$\delta = \frac{\tfrac{1}{2}m_i v_r^2 - 0.15\,\mu f_g (\sigma_n - \sigma_{ni})}{\mu f_g \sigma_{ni} + m_i g \dfrac{\tau_d}{\tau_r} \sin\beta} \qquad (47)$$

Each of these three displacement equations was applied to the five documented relative displacements from MIGHTY EPIC listed in Table 4. A coefficient of friction μ of 0.55 was used throughout. This cor-

responds to a friction angle of 29°, which is the lowest limit computed in the shear stress analysis of the MIGHTY EPIC relative displacements. The computed area coefficients, in situ normal stress and shear stress ratios are listed in Table 4, but, because of classification restrictions, the values of mass increments, peak normal stresses and peak velocities are omitted. The displacements computed using each of the three models are listed along with the actual displacements. Overall, model 2 (eq 46), which assumes that the dynamic component of normal stress dissipates over half the total displacement, gives the best agreement with the measurements. All values of computed displacement using this method fall within about 40% of the actual values.

DIABLO HAWK PREDICTIONS

The DIABLO HAWK relative displacement predictions are based on the MIGHTY EPIC analysis outlined in the previous section. Like that analysis, it is divided into two parts. The first part includes a shear stress analysis which computes the anticipated magnitudes and directions of the peak shear stresses at each DIABLO HAWK fault documentation location and compares these to the predicted shear strengths. At locations where the predicted shear stress exceeds the shear strength, relative displacement is predicted in the direction of the peak shear stress. The second portion of the analysis is then applied only at these locations to predict the magnitude of the relative displacements.

Figure 23 is a plan view of all passive fault documentation locations on DIABLO HAWK. The faults are identified by the drift in which they are located, according to the system used by Kipp and Kennedy (1978). The strike, dip, radial distance and direction from the working point of the faults at each documentation station are listed in Table 5. In instances where the faults can be identified as part of a major throughgoing fault, they are also listed by the number of the major fault adjacent to the drift identification number.

The passive fault documentation, prepared by the U.S. Geological Survey, consists of four steel pins glued in the form of a parallelogram into the drift wall as shown schematically in Figure 24. Two pins are located on each side of the fault, roughly parallel to it. This arrangement is duplicated on the opposite wall of the drift, making a total of eight pins at each fault intersection. The 28 different pin to pin dimensions are recorded before and after the test. Triangulation is used to determine the strike and dip components of any relative displacement.

19
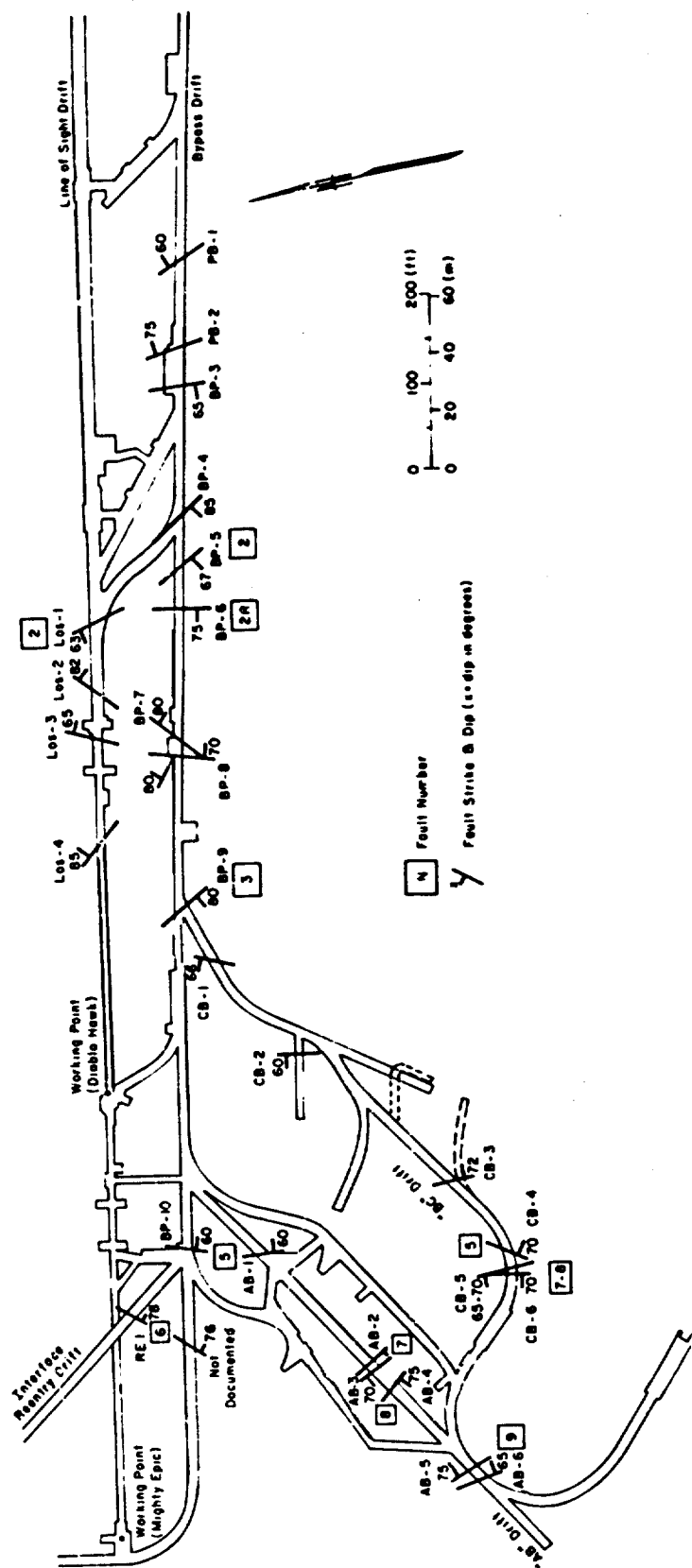
Figure 23. Location of DIABLO HAWK fault documentation stations (from Short and Kennedy, 1978).

Table 4. MIGHTY EPIC calculated displacements.

Location	Area Coefficient I_y	In situ normal stress σ_{ni} (bars)	Shear stress ratio (τ_i/T_i)	Calculated displacement (m)			Actual displacement (m)
				Model 1	Model 2	Model 3	
Fault S B drift	1.33	55.7	-0.28	0.37	0.66	0.61	0.46
Fault S Bypass drift	1.19	58.4	-0.90	0.44	0.78	1.31	0.67
Fault near fault 6 – LOS drift	1.22	61.5	1.0	0.66	1.22	4.32	>1.68
3RC/3D bedding plane	4.75	78.3	-0.80	0.64	0.73	0.76	>0.91
Fault through Interface drift	2.65	47.0	-0.12	0.53	0.73	0.79	≥0.88
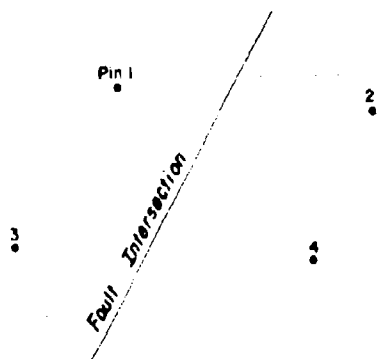
Figure 24. Schematic side view—typical passive fault documentation station.

The determination of the peak shear stresses at each fault documentation location follows the technique outlined in the previous section. The predicted peak values of strike shear, dip shear and normal stress were determined using eq 23, 24 and 25 respectively. The peak principal stresses used in these equations were computed by superimposing the critical dynamic stresses on the in situ stress approximation for Rainier Mesa. As in the MIGHTY EPIC analysis, the critical dynamic stress state was assumed to be the peak radial stress given in Figure 13 acting simultaneously with zero tangential stress. The superposition was done using Mohr circles. In addition to the peak principal stresses, the Mohr circle analysis also yielded values for the angle θ required for the solution of eq 23-25 at each location. The peak strike and dip shear stresses were substituted into eq 6 to give the resultant total shear stress acting in the direction γ as listed in Table 5. The peak normal stresses were substituted into eq 5 to obtain the critical shear stresses (anticipated shear strengths) at each location. The parameters obtained from the DIHEST and MIGHTY EPIC analyses (i.e., a cohesion τ_0 of 10 bars and a friction angle of $29°$) were used to calculate τ_c. The rationale in employing these values, discussed in detail in the previous section, was that 10 bars appeared to approximate the lower bound of an extrapolation of the DIHEST results to nuclear and high explosive surface bursts, and the friction angle of $29°$ is the computed *maximum* value which would have permitted *all* the displacements observed on MIGHTY EPIC to occur. The ratios of the peak shear stress to the critical shear stress, τ_r/τ_c, are listed in Table 5. For values greater than 1.0, the total shear stress exceeds the computed shear strength and relative displacement is predicted. The stress ratio may be indicative of the probability of displacement occurrence. Higher ratios

would indicate a higher likelihood of displacement than ratios closer to 1.0. Of the faults that are not predicted to move, those with a ratio close to 1.0 would have a higher likelihood of displacing than those with lower stress ratios. Again, because of classification restrictions, the actual values of shear stresses and normal stresses are not included in the table.

Displacement predictions were made for the 14 fault documentation stations with stress ratios greater than 1.0 using eq 46, which gave the best fit to the MIGHTY EPIC data of the three displacement models examined. The computed area coefficients f_g, in situ normal stresses σ_{ni} and dip shear stress to total stress ratios τ_d/τ_r are listed in Table 5. The remaining input parameters are not listed because of classification restrictions. The 14 total displacement predictions are listed along with a breakdown of their strike and dip components. The strike and dip components are computed with the assumption that motion will be in the direction of the resultant shear vector τ_r. Negative dip slip values indicate that the block on the working point side of the fault moves downward relative to the opposite block. RL and LL indicate right lateral or left lateral strike slip displacement. The predicted magnitude of total displacement ranges from 0.15 m at BP-4 to 1.83 m at BP-9. The shear stress ratios for several of the faults for which displacement is predicted, such as BP-4 and RE-1, are close enough to 1.0 that it would not be surprising if no relative motion occurred. On the other hand, there are several faults, such as LOS-3 and AB-6, for which no displacement is indicated. But they have stress ratios close to 1.0 and might easily exhibit relative displacement.

In summary, the DIABLO HAWK predictions are based on semi-empirical equations derived from the combined MIGHTY EPIC and DIHEST experience. The estimated peak shear stress acting on each fault is compared to the estimated shear strength to determine whether slip will occur. Both estimates are based on approximations of the combined in situ stress and dynamic loadings. If slip is predicted, the magnitude of displacement is computed from an equation based on the dissipation of the kinetic energy for an increment of mass extending radially from the cavity wall to the fault. The equation considers energy dissipated by friction along the fault during displacement and the loss or gain in energy associated with changes in elevation of the block. Both the coefficient of sliding friction and the normal stress distribution on the fault during the course of the relative motion are based on analyses of the MIGHTY EPIC data.

Obviously, the principal inadequacy of these prediction techniques is that they do not treat the faults and blocks making up the in situ mass as continuous.

21

Table 5. DIABLOW HAWK displacement predictions.

Documentation station	Major fault no.	Range (m)	Strike	Dip	Direction from W.P.	τ_r/τ_c	γ (deg)	t_g	σ_{ni} (bars)	τ_d/τ_r	Predicted displacement (m)		
											δ_s strike*	δ_d dip	δ Total
LOS-1	2	162	N18W	63SW	S79E	0.94							
LOS-2		135	N50E	82SE	S79E	1.21	- 8.6	1.35	40.3	-0.15	0.51 RL	-0.08	0.52
LOS-3		119	N28E	65SE	S79E	0.90							
LOS-4		85	N43W	85NE	S79E	2.06	- 3.4	1.67	80.0	-0.06	1.07 LL	-0.06	1.07
BP-1		287	N25W	60NE	S72E	0.54							
BP-2		256	N9W	75NE	S72E	0.41							
BP-3		242	N2E	65SE	S71E	0.46							
BP-4		196	N34W	85SW	S70E	1.04	4.0	1.56	78.6	0.07	0.15 LL	0.01	0.15
BP-5	2	180	N29W	67SW	S70E	1.16	19.7	1.66	77.4	0.33	0.14 LL	0.05	0.15
BP-6	2B	165	N11E	75NW	S69E	0.40							
BP-7		120	N51E	80SE	S66E	0.86							
BP-8		115	N19E	70NW	S65E	0.57							
BP-8A		115	N45W	80NE	S66E	2.47	- 3.4	2.71	80.0	-0.06	0.54 LL	-0.03	0.54
BP-9	3	66	N34W	80SW	S56E	3.59	4.0	2.77	78.6	0.07	1.82 LL	0.13	1.82
BP-10	5	62	N20E	60SE	S76W	1.68	35.5	1.40	55.4	0.58	1.29 RL	0.92	1.58
RE-1	6	79	N39E	79SE	N84W	1.19	17.5	1.23	42.2	0.30	1.20 RL	0.35	1.15
AB-1	5	78	N5E	60SE	S60W	1.62	35.5	1.40	62.4	0.58	0.96 RL	0.68	1.18
AB-2	7	128	N29W	65SW	S58W	0.71							
AB-3	8	132	N24W	70SW	S58W	0.62							
AB-4	8	141	N40W	75SW	S58W	0.44							
AB-5	9	180	N21W	75NE	S58W	0.49							
AB-6	9	184	N10W	65NE	S58W	0.85							
CB-1		58	N24E	68NW	S39E	1.18	6.2	1.21	50.0	0.59	1.21 LL	0.88	1.50
CB-2	4	67	N8E	80NW	S1E	4.86	0.0	8.97	55.3	0.0	1.36 LL	0.0	1.36
CB-3		120	N2W	72NE	S27W	2.35	8.0	2.10	63.2	0.14	0.55 RL	0.08	0.56
CB-4	5	148	N34E	70SE	S34W	0.42							
CB-5	7,8	151	N11W	67SW	S36W	1.47	-19.3	1.49	69.4	-0.33	0.33 RL	-0.12	0.35
CB-6	7,8	152	N5E	70NW	S37W	1.93	- 8.6	1.95	59.3	-0.15	0.34 RL	-0.05	0.34

* RL is right lateral strike slip displacement; LL is left lateral displacement.

For instance, in Figure 23 the faults labeled BP-10, AB-1 and CB-4 are all segments of the major fault 5. At documentation stations BP-10 and AB-1 substantial slip is predicted. Yet at station CB-4, because the fault strike has changed so that it trends directly toward the working point, motion is not predicted. In fact, the shear stress ratio is very low, which would normally be taken to mean that the probability of displacement is also very low. However, if substantial displacement occurs as predicted at both BP-10 and AB-1 it would seem likely that this would carry through to CB-4 unless some other intervening fault provided a more convenient release for this motion. Likewise, the magnitude of displacement at one point within a displaced fault block cannot be independent of the magnitude at another point within that same block, if the block remains intact between the two points. In other words, if a meter of slip were to occur at BP-10 and AB-1 due to displacement of the block on the working point side of fault 5 a similar amount of displacement would be expected at CB-4, assuming that the slip block is an intact block and that residual compression of the block is negligible.

Unfortunately, it appears impossible to adequately describe the complete geometry of the planes of weakness and blocks surrounding a detonation, let alone the intricate details of their interactions during relative displacement. In many instances a potential slip plane would only be encountered at one point by an excavation. The directions of the extension of this plane and the existence of other interacting planes could only be determined through costly and elaborate exploration programs. Even with the most complete exploration programs there are often structural weaknesses of critical importance that go undetected. In other words, it appears unlikely that a reliable quantitative model which accurately describes detailed block motion behavior can be developed in the near future because the analysis tools are inadequate for the three-dimensional job and the geologic exploration necessary to completely describe a site would be prohibitively expensive. Perhaps a semi-empirical approach, coupled with a probabilistic analysis based on our expanding data base, will prove adequate.

22

LITERATURE CITED

Bache, T.C. and D.G. Lambert (19. 5) The seismological evidence for the triggering of block motion by large explosions. LaJolla, California: Systems, Science and Software.

Blouin, S.E. (1980) Block motion from detonation of buried arrays. U.S. Army Cold Regions Research and Engineering Laboratory, CRREL Report 80-26.

Butters, S.W. (1976) Characterization of tuff and development of grouts for MIGHTY EPIC structures program, TR 76-21. Salt Lake City, Utah: Terra Tek.

Crawford, R.E., C.J. Higgins, and E.H. Bultmann (1974) The Air Force manual for design and analysis of hardened structures, AFWL-TR-74-102, Albuquerque, New Mexico: Civil Nuclear Systems Corporation.

Ellis, W.L. (1976) Representative values for the in situ state of stress within Rainier Mesa, Nevada Test Site, USGS letter to H.L. McKague. Denver, Colorado: United States Department of the Interior, Geological Survey.

Kipp, T.R. and B.P. Kennedy (1978) Interim report 2, MIGHTY EPIC/DIABLO HAWK block motion program, documentation of the DIABLO HAWK block motion instrumentation. Irvine, Calif: Engineering Decison Analysis Co., Inc.

Rinehart, J.S. (1975) Stress transients in solids. Sante Fe, New Mexico: Hyper Dynamics.

Ristvet, B.L., E.L Tremba, R.F. Couch, Jr., J.A. Fetzu, E.R. Goth, D.R. Walter and V.P. Wendland (1978) Geological and geophysical investigations of the Eniwetok nuclear craters. Air Force Weapons Laboratory, AFWL-TR-77-242.

Selberg, H.L. (1951) Transient compression waves from spherical and cylindrical cavities. *Arkiv fur Fysik*, vol. 5, p. 97.

Short, S.A. and R.P. Kennedy (1978) Interim report 1, MIGHTY EPIC/DIABLO HAWK block motion program, block motion phenomena during MIGHTY EPIC. Irvine, California: Engineering Decision Analysis Co., Inc.

Timoshenko, S. and J.N. Goodier (1970) *Theory of elasticity*, 3rd ed. New York: McGraw Hill Book Co., Inc.

Townsend, D.R. (1976) MIGHTY EPIC reentry geologic observations. Mercury, Nevada: United States Department of the Interior, Geological Survey.

Townsend, D.R. (1977a) Shock induced fault movement in the MIGHTY EPIC "A" structures drift. Mercury, Nevada: United States Department of the Interior, Geological Survey.

Townsend, D.R. (1977b) Shock induced fault movement in the MIGHTY EPIC Interface drift. Mercury, Nevada: United States Department of the Interior, Geological Survey.

Townsend, D.R. (1977c) Shock induced fault movement in the MIGHTY EPIC LOS drift. Mercury, Nevada: United States Department of the Interior, Geological Survey.